NANO LETTERS

Letter

pubs.acs.org/NanoLett

Tuning Oxygen Reduction Reaction Activity via Controllable Dealloying: A Model Study of Ordered Cu_3Pt/C Intermetallic Nanocatalysts

Deli Wang,[†,∇] Yingchao Yu,[†,∇] Huolin L. Xin,[‡,#] Robert Hovden,[⊥] Peter Ercius,[§] Julia A. Mundy,[⊥] Hao Chen,[†] Jonah H. Richard,[∥] David A. Muller,[⊥,¶] Francis J. DiSalvo,[†,*] and Héctor D. Abruña[†,*]

[†]Department of Chemistry and Chemical Biology and [‡]Department of Physics, Cornell University, Ithaca, New York 14853, United States

[§]National Center for Electron Microscopy, Lawrence Berkeley National Laboratory, Berkeley, California 94720, United States

[∥]Department of Physics, Bard College, Annandale-On-Hudson, New York 12504, United States

[⊥]School of Applied and Engineering Physics and [¶]Kavli Institute, Cornell University, Ithaca, New York 14853, United States

Supporting Information

ABSTRACT: A promising electrocatalyst prototype of low Pt mole fraction, intermetallic nanoparticles of Cu_3Pt, has been prepared using a simple impregnation-reduction method, followed by a post heat-treatment. Two dealloying methods (electrochemical and chemical) were implemented to control the atomic-level morphology and improve performance for the oxygen reduction reaction (ORR). The morphology and elemental composition of the dealloyed nanoparticles were characterized at angstrom resolution using an aberration-corrected scanning transmission electron microscope equipped with an electron energy loss spectrometer. We found that the electrochemical dealloying method led to the formation of a thin Pt skin of ca. 1 nm in thickness with an ordered Cu_3Pt core structure, while chemical leaching gave rise to a "spongy" structure with no ordered structure being preserved. A three-dimensional tomographic reconstruction indicated that numerous voids were formed in the chemically dealloyed nanoparticles. Both dealloying methods yielded enhanced specific and mass activities toward the ORR and higher stability relative to Pt/C. The spongy nanoparticles exhibited better mass activity with a slightly lower specific activity than the electrochemically dealloyed nanoparticles after 50 potential cycles. In both cases, the mass activity was still enhanced after 5000 potential cycles.

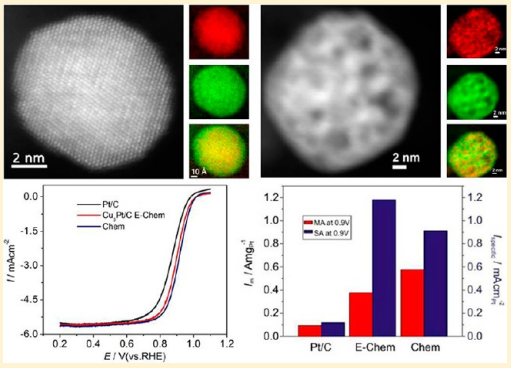

KEYWORDS: *Fuel cell, ORR, electrocatalyst, ordered intermetallic nanoparticle, dealloying*

Proton exchange membrane fuel cells (PEMFCs) have long been considered as a potential green alternative to internal combustion engines used in automotive and stationary applications due to the potential for high efficiencies (as they are not limited by the Carnot cycle) and zero carbon dioxide emissions when hydrogen is the fuel.[1,2] One of the major limitations for commercialization of this technology is the high cost of Pt, which is used as the electrocatalyst in the anodes and cathodes of fuel cells. Numerous studies have been dedicated to screening more efficient electrocatalytic materials, especially for lowering the precious metal loading and improving the sluggish kinetics of the oxygen reduction reaction (ORR) at the cathode. Early studies focused on lowering cost and improving ORR activity by alloying Pt with some 3d transition metals (i.e., Pt−M alloys, where M = Fe, Co, Ni, V, and so forth),[3−9] and the activities of these materials have been found to be about 2−4 times greater than pure Pt for the ORR.[8,10−14] Other approaches have included Pt monolayer catalysts on nanoparticles of other metals or metal oxides[15−17] and different single crystal planes, such as Pt(110),[18] Pt(100),[18] and Pt_3Ni(111),[19] and so forth.

Recently, dealloyed Pt bimetallic nanoparticles, especially Pt−Cu alloy nanoparticles, have attracted attention as electrocatalysts for the ORR.[20−26] It has been shown that by using electrochemical methods, Cu is removed from the alloy surface layers, forming a Pt-rich core−shell nanostructure, which exhibits enhanced ORR activity when compared to pure Pt nanoparticles.[22−24] Most previous studies have focused on Pt-based alloy nanoparticles in which the lack of an ordered structure makes it more challenging to produce a specific atomic-level morphology and surface structure.[27,28] Here we explore ordered intermetallic Cu_3Pt/C nanoparticles as a promising type of a low Pt-content electrocatalyst, which can be prepared using a simple impregnation-reduction method

Received: June 28, 2012
Revised: August 28, 2012
Published: September 6, 2012

   dx.doi.org/10.1021/nl302404g | *Nano Lett.* 2012, 12, 5230−5238

followed by a high-temperature post-treatment. Two dealloying methods were examined to enhance the ORR activity, namely, electrochemical and chemical leaching. The morphology and

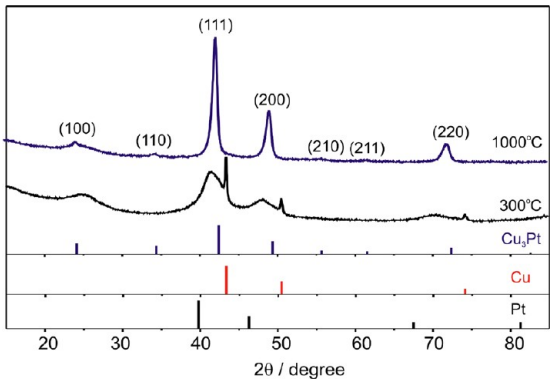

Figure 1. XRD patterns of Cu_3Pt/C prepared at 300 °C and after 1000 °C heat-treatment. Below are the peak positions of standard pure metallic Pt, Cu, and intermetallic Cu_3Pt.

atomic-scale elemental distribution of the as-prepared and dealloyed nanoparticles were determined using atomic-resolution electron energy loss spectroscopic (EELS) imaging in a fifth-order aberration-corrected scanning transmission electron microscope (STEM) equipped with an electron energy loss spectrometer. Using atomic-scale EELS mapping, we found that both Pt and Cu are distributed relatively uniformly in the as-prepared particles, and that the surfaces do not show significant preferential segregation. After electrochemical dealloying, an ~1 nm Pt-rich shell is formed enclosing an ordered Cu_3Pt intermetallic core. The ordered core strains the Pt shell, which is known to enhance the electrocatalytic activity toward the ORR.[7] Unlike electrochemical dealloying, however, chemical leaching gave rise to a "spongy" structure with no apparent remaining ordered intermetallic structure, which was further verified by a three-dimensional (3D) tomographic reconstruction. This study reveals the correlations among the dealloying treatments, the resulting atomic-scale chemical structure, and ORR activity.

Carbon-supported Cu_3Pt intermetallic nanoparticles with 10% Pt by weight, 10 wt %, were prepared via a two-step route (Supporting Information Figure S1). First, the Cu_3Pt/C nanoparticles were preprepared using an impregnation-reduction method in which the H_2PtCl_6 and $CuCl_2$ precursors (previously adsorbed on the Vulcan XC-72 support) were reduced under flowing H_2 in a tube furnace at 300 °C. The sample was then annealed at 1000 °C in a tube furnace under flowing H_2 to form an ordered intermetallic phase. Figure 1 shows the X-ray diffraction (XRD) patterns of the samples and the standard powder diffraction files (PDF). When annealed at 300 °C, two types of diffraction peaks were present: broad peaks with characteristic at 2θ values of 41, 48, and 70° and sharp ones at 2θ values of 43, 50, and 74°. The broad diffraction peaks were at higher angles, compared to pure Pt, because the lattice contracts when Cu atoms are incorporated into the Pt lattice to form a $PtCu_x$ alloy. The sharp diffraction peaks, corresponding to metallic Cu, indicate that not all of the Cu was alloyed with Pt under the experimental conditions employed. On the other hand, the single phase, ordered intermetallic Cu_3Pt, formed after the as-prepared $PtCu_x$-Cu/C nanoparticles were heat-treated at 1000 °C (Figure 1). The XRD pattern showed pronounced (100) and (110) superlattice peaks, characteristic of a well-ordered, intermetallic phase, and all the diffraction peak positions were consistent with the standard PDF card of the Cu_3Pt intermetallic phase (PDF card #03-065-3247). The average particle size calculated by using the Debye–Scherrer equation is about 12 nm. We also performed an in situ transmission electron microscopy (TEM) heating experiment to monitor changes to the as prepared (at 300 °C) $PtCu_x$–Cu nanoparticles upon annealing at higher temperatures (Supporting Information Figure S2). After heating at 1000 °C, the large Cu particles decreased in

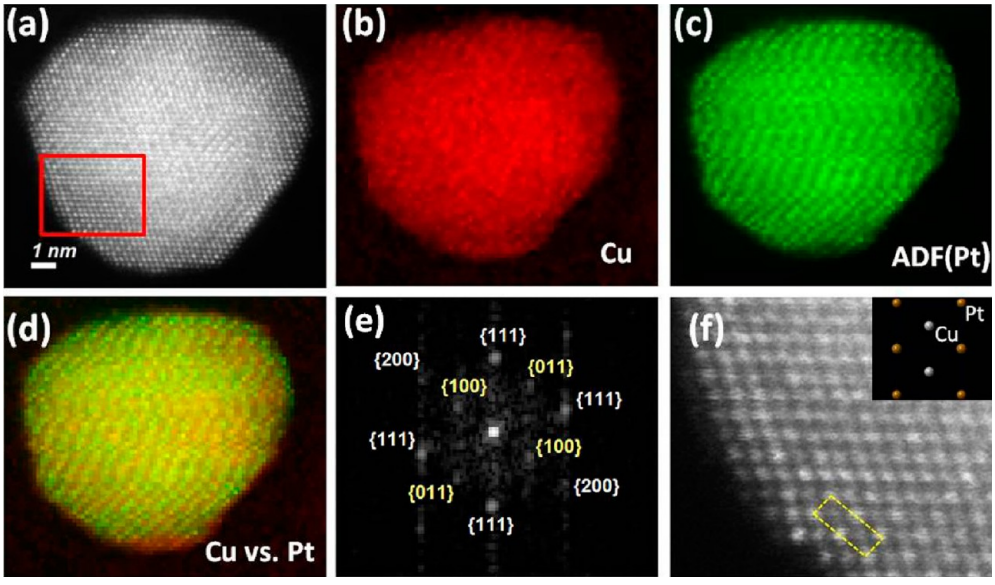

Figure 2. (a) ADF-STEM images of a [011] oriented Cu_3Pt/C intermetallic nanoparticle; (b) 2D EELS map of Cu-$L_{2,3}$ edge; (c) simultaneously recorded ADF image, which represents signals from Pt due to Z-contrast; (d) composite Cu vs Pt map, showing a homogeneous distribution of Pt and Cu; (e) FFT of (a) with {100} peak indicating formation of intermetallic structure; (f) a crop of the super lattice feature from (a) with four Pt atoms (brighter) around each Cu atom (darker). The matching theoretical model of ordered intermetallic Cu_3Pt is shown in the inset of (f).

dx.doi.org/10.1021/nl302404g | *Nano Lett.* 2012, 12, 5230–5238

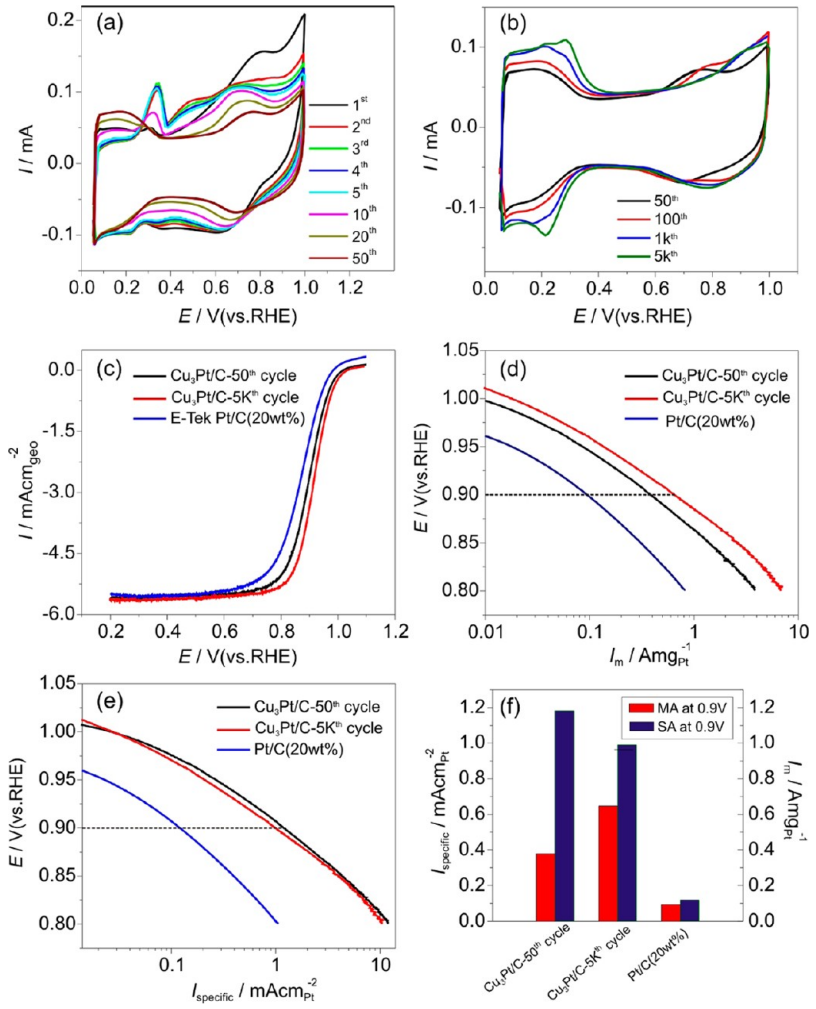

Figure 3. (a,b) Cyclic voltamograms of Cu_3Pt/C ordered intermetallic nanoparticles during electrochemical dealloying in 0.1 M $HClO_4$, at a scan rate of 50 mV s^{-1}. Color-coded legends indicate the cycle number. (c) ORR polarization curves in O_2-saturated 0.1 M $HClO_4$ at a rotation rate of 1600 rpm and a scan rate of 5 mV s^{-1}. (d,e) Pt mass and area specific activities at +0.9 V, respectively. (f) Summary of mass and specific activities for the ORR.

size and disappeared, while the smaller particles of $PtCu_x$ grew concomitantly larger.

Energy-dispersive X-ray (EDX) and EELS elemental mapping are invaluable tools for understanding the composition and morphology of Pt-bimetallic nanoparticles.[22,29−32] Figure 2a,b shows the scanning TEM (STEM)-EELS images of a Cu_3Pt/C nanoparticle, while the EELS mappings of Cu and Pt are shown in Figure 2b−d. The images indicate that there is no phase segregation of Cu and Pt in the core, while one to two monolayers of Cu are segregated on four facets, while others are Pt−Cu alloy terminated. Evidence of Cu on the surface could also be found in the cyclic voltammetric (CV) testing in Figure 3a, vide infra. The Fourier fast tranform (FFT) analysis (Figure 2e) exhibited three groups of diffraction peaks, {111}, {100}, and {200}, which are in agreement with the XRD results. The strong intensity of the {100} and {110} peaks is evidence of the existence of an ordered structure across the selected region. The "Z-contrast" image obtained with an annular dark field (ADF) was used to differentiate between columns of Pt and Cu atoms in appropriately oriented particles. The ADF detector collects elastically scattered electrons with an intensity that is 5−7 times higher for Pt than for Cu, allowing the differentiation of Pt and Cu atoms based on the intensities in a ADF-STEM image.[33] The box in Figure 1f demonstrates that there are periodic square arrays of four Pt atoms around each Cu atom, which is consistent with the ordered structure (inset in Figure 2f). All of these observations unambiguously indicate the formation of ordered intermetallic Cu_3Pt nanoparticles.

Two methods were used to dealloy the Cu_3Pt/C intermetallic nanoparticles. In the first, the potential applied to the Cu_3Pt/C intermetallic nanoparticles was cycled between +0.05 and +1.0 V (Figure 3a,b). The first five cycles exhibited no clear hydrogen adsorption/desorption peaks between +0.05 and +0.3 V, indicating that the surface is not Pt-rich. In addition, at the second cycle it was apparent that some Cu had dissolved into the solution during the first anodic scan, as indicated by the small bulk Cu oxidation peak at around +0.3 V, and the broad peak between +0.3 to +0.9 V due to the under potential deposition of Cu. In the cathodic scan, Cu was redeposited on the nanoparticles, as evidenced by the three peaks at +0.6, +0.35, and +0.25 V. As the cycling continued, the Cu peaks gradually decreased and hydrogen adsorption/desorption features emerged and became well-defined after 50 cycles, indicating that the surface had become Pt-rich. In addition, both the onset potential and the peak potential of the

dx.doi.org/10.1021/nl302404g | Nano Lett. 2012, 12, 5230−5238

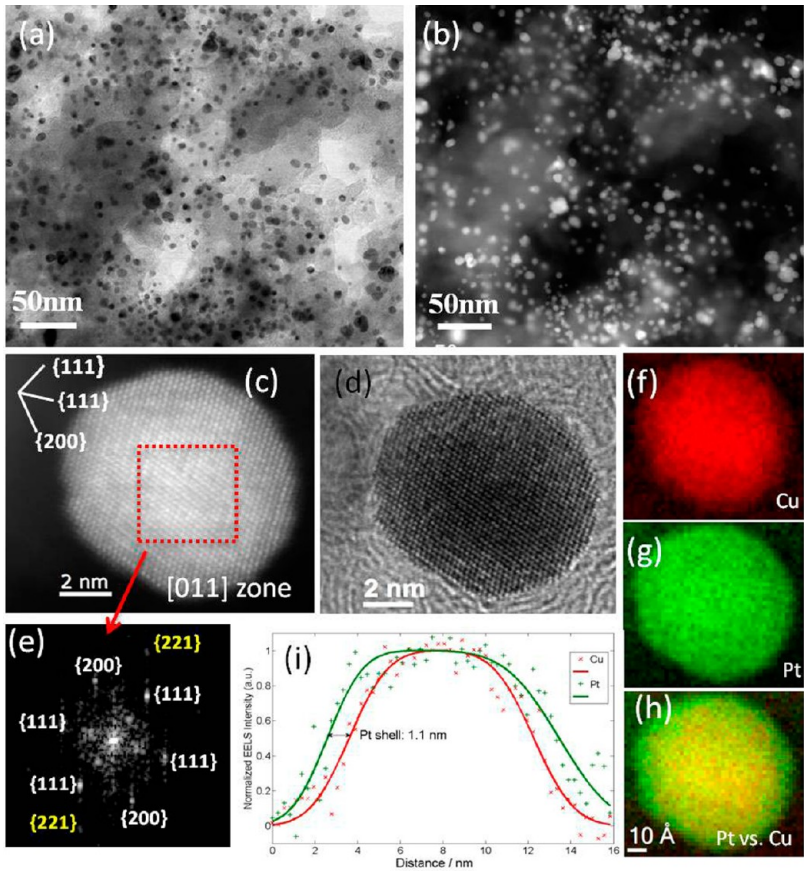

Figure 4. (a,b) BF and ADF-STEM overview images of Cu_3Pt/C intermetallic nanoparticles after electrochemical dealloying. (c,d) Atomic-resolution HAADF-STEM and BF images of one nanoparticle along [011] zone axis, showing an ordered intermetallic structure in the highlighted region. (e) FFT of highlighted area from (c) with superlattice peaks in red. (f) EELS mapping of Cu $L_{2,3}$ edge. (g) EELS mapping of Pt N_3 edge after 20 iterations of MCR (multivariate curve resolution) analysis (a comparison on the reliability of such method is in Supporting Information Figure S6). (h) Combination of (f) and (g), showing Pt shell. (i) Line profiles of Pt and Cu with a quantitatively determined 1.1 nm Pt shell.

Pt oxide reduction shifted in positive direction with cycling, reflecting a decrease in the adsorption strength of the oxygen-containing species on the electrode surface, which is key for enhancing the ORR activity.[34,35]

After rinsing the electrode and placing it in fresh, O_2-saturated electrolyte, the electrocatalytic activity for ORR of electrochemically dealloyed Cu_3Pt/C intermetallic nanoparticles was investigated by linear sweep voltammetric (LSV) scans using a rotating disk electrode (RDE) (Figure 3c). Compared to Pt/C catalyst nanoparticles, the ORR polarization curves of dealloyed Cu_3Pt/C intermetallic nanoparticles exhibited onset and half wave potentials that were 40 mV more positive after 50 potential cycles, and even more positive (for a total about of 50 mV) after 5000 cycles. The Pt mass activity at +0.9 V was determined to be 0.38 and 0.65 A/mg_{Pt} after 50 and 5000 cycles, respectively. These values are about five and seven times higher than that of the Pt/C catalyst (Figure 3d,f). The specific activity (current per unit surface area of Pt as determined by hydrogen adsorption) also showed a 1 order of magnitude increase (Figure 3e) relative to Pt/C. The current density was obtained by normalizing the kinetic current to the Pt surface area that was calculated by integrating the coulometric charge associated with the adsorption and desorption of hydrogen between +0.05 and +0.40 V, using a conversion factor of 200 $\mu C\ cm^{-2}$ for the adsorption of a monolayer of hydrogen (the value of 200 $\mu C\ cm^{-2}$ was recently proposed by Feliu et al.[36,37]). Such enhanced activity could be ascribed to two reasons (1) the formation of a large number of active sites after dealloying (Figure 3b) and (2) the modification of the electronic structure of Pt. Both effects would affect the bonding energy between Pt and oxygen-containing species (Figure 3b).

Figure 4a,b shows a pair of overview STEM images of Cu_3Pt/C intermetallic nanoparticles after electrochemical dealloying. The images show that a majority of the particles are still well-dispersed on the carbon support and the particle size distribution calculate from more than 100 nanoparticles shows that the mean particle size is about 11 nm in diameter, which is comparable to the as-prepared nanoparticles (Supporting Information Figure S3). One representative nanoparticle was investigated by atomic resolution imaging (Figure 4c,d). The intermetallic core structure was preserved after the electrochemical dealloying treatment, as seen from the ADF-STEM images (Figure 4c,d), and the FFT indicates the presence of superlattice peaks such as {221} (Figure 4e). The surface of this nanoparticle is Pt-rich, as demonstrated by EELS mapping (Figure 4f–h), and consistent with the cyclic voltammetric measurements. Since the Cu-$L_{2,3}$ edge has very distinct features and an abrupt onset, a linear combination of power-law background subtraction method was used[38] (Figure 4f) to separate out the Cu edge. On the other hand, the delayed onset for Pt–N and Pt–M edges is highly sensitive to errors in the power-law background subtraction. To map Pt concentrations accurately (Figure 4g), the multivariate curve

dx.doi.org/10.1021/nl302404g | Nano Lett. 2012, 12, 5230–5238

resolution (MCR) method was carried out on the Pt−N edge (the evaluation of such method is presented in Supporting Information Figure S4 and can also be found in a previous publication[29]). This method enables a clear determination of the Pt-shell thickness to be about 1 nm (Figure 4i).

Chemical dealloying of the Cu_3Pt/C ordered intermetallic nanoparticles was carried out by immersing the sample in 1 M HNO_3 for 2 days under continuous magnetic stirring. XRD showed that after chemical dealloying, all the peaks became weaker and their peak positions shifted to lower angles, although still not as low as the peak positions of pure Pt (Supporting Information Figure S5), indicating the partial but not total, removal of the Cu from the bulk of the Cu_3Pt/C ordered intermetallic nanoparticles. The super lattice peaks characteristic of the ordered intermetallic structures at around 24 and 34° are almost invisible, indicating that a disordered Pt_xCu alloy formed after chemical dealloying. The overview of bright-field (BF) and ADF-STEM images (Figures 5a) show

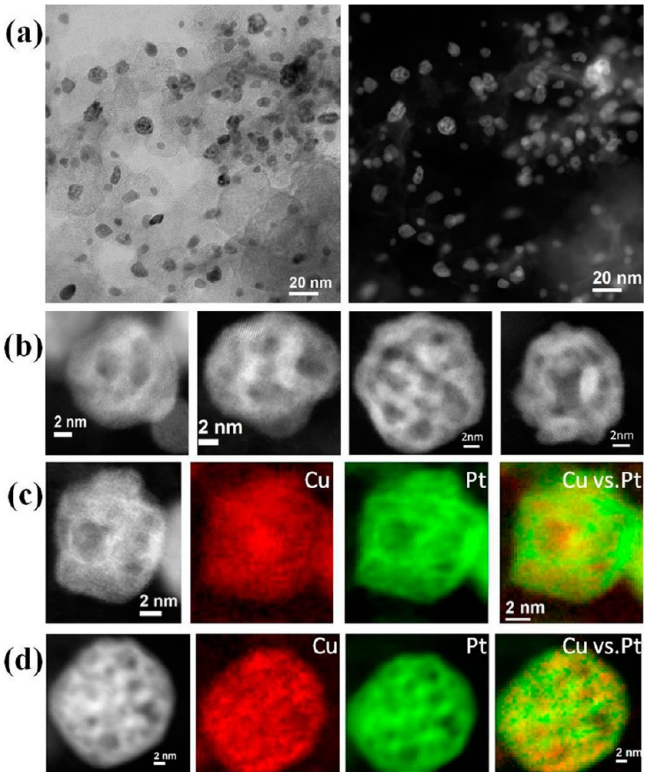

Figure 5. (a) BF (left) and ADF-STEM (right) overview images of Cu_3Pt/C intermetallic nanoparticles after chemical dealloying. (b) Atomic-resolution BF-STEM image of four spongy nanoparticles. (c,d) EELS mapping of Cu $L_{2,3}$ edge and simultaneously recorded Pt $M_{4,5}$ edges and combination of Cu and Pt maps, showing two nanoparticles of approximately 10 and 20 nm, respectively.

that the particles are well distributed on the carbon support. The speckle patterns in the Z-contrast (ADF-STEM) images (Figures 5a (right) and 5b) of the chemically dealloyed particles indicate that the particles may have developed a porous structure. However, the origin of the dark spots in the projected Z-constrast images could either reflect Cu-rich volumes (Cu scatters less than Pt) or voids/divots (deficiency of both Pt and Cu). The presence of Cu-rich volumes, nonetheless, can be excluded by our chemical mapping of the particles (Figure 5c,d). From a comparison of the Z-contrast dark spots and the Cu and Pt elemental maps, there does not appear to be any correlation. Thus, although a bit speculative on our part, we believe that the dark features in the image represent voids in the nanoparticles, consistent with a spongy structure. To directly visualize the three-dimensional porous network formed after chemical dealloying, we performed ADF-STEM 3D tomography of spongy nanoparticles. The reconstructed porous structures are visualized in Figure 6. Two differential viewing angles are provided (Figure 6a,b) with two arrows indicating channels connecting to the exterior surfaces. The internal porous network is visualized from consecutive cross-sectional images through the 3D reconstruction of the nanoparticle (Figure 6c). It demonstrates the internal nanoporosity of the nanoparticles and a dramatic increase in the surface-to-volume ratio after the chemically dealloying process. The formation of the spongy structures is likely due to the Kirkendall effect (the diffusion rates of Pt and Cu are different in the alloy) similar to the previously reported hollow-structure formation.[39]

To evaluate the effects of size on the morphology of chemically dealloyed nanoparticles,[40] we analyzed the size distributions of spongy nanoparticles (Figure 7). Since only a fraction of the nanoparticles are on the same focal plane from the HAADF-STEM image (Figure 5a), analyzing nanoparticles from these images will introduce inaccuracies, especially when many of the pores are almost invisible when outside the depth of focus. Therefore, we have carried out an experiment in which we take 34 consecutive images at different defocus, a procedure that has been previously reported to be more accurate for analyzing nanoparticle size distribution.[41] By extend depth of field reconstruction,[42] most nanoparticles are present on the same focal plane (Figure 7a). The size distribution of such an image is shown in Figure 7b, where the "nonspongy" nanoparticles have a mean diameter of 7.5 ± 0.7 nm while the spongy ones are 14.9 ± 2.4 nm. We checked the accuracy of the method by hand-segmentation of nonspongy and spongy particles separately (Figure 7c,d). However, since not all the pores are observable at the same viewing direction, it is possible that we might pick (place) some spongy ones into the nonspongy category. The analysis of such error is propagated by reporting the upper bound of the number of nonspongy ones and the lower bound for the spongy ones. As Figure 5a shows, after chemically dealloying only the larger size nanoparticles have evolved into porous structures, while most of smaller ones remain nonspongy. In the case of Pt−Cu binary materials, since Cu is more soluble than Pt upon electrochemical cycling, vacancies are expected inside the particles, if a Pt-rich shell is formed on the surface, so as to slow further diffusion. A spongy structure could evolve when the etching rate of Cu is comparable to the surface diffusion rate of Pt.[29,43] However, if the diffusion length (where Pt is redeposited on the surface) is larger than the particle size, a spongy structure would not be expected.[29,40,43] This explains why many smaller nanoparticles have remained nonspongy after chemical dealloying, and in turn, illustrates the importance of using through-focal ADF-STEM imaging series and EELS mapping to confirm the existence of porous structures. Similar results have been recently reported in a study of the size dependence of structure and morphology in dealloyed bimetallics in which it was shown that nanopores or hollows were not observed when the particle size was below 5 nm, while multiple core−shell structures formed when the particle size ranged up to 20 nm.[40]

dx.doi.org/10.1021/nl302404g | Nano Lett. 2012, 12, 5230−5238

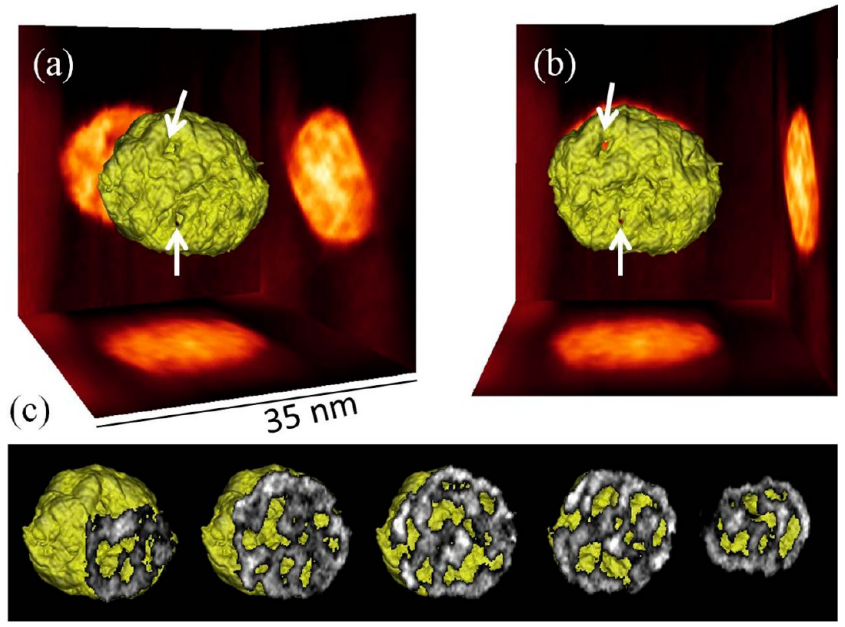

Figure 6. (a,b) Three-dimensional tomographic reconstruction of a chemically dealloyed nanoparticle (spongy) at two different viewing directions. The arrows indicate channels connecting to the exterior surfaces. (c) A series of consecutive slices through the isosurfaces of such nanoparticle, showing the porous networks.

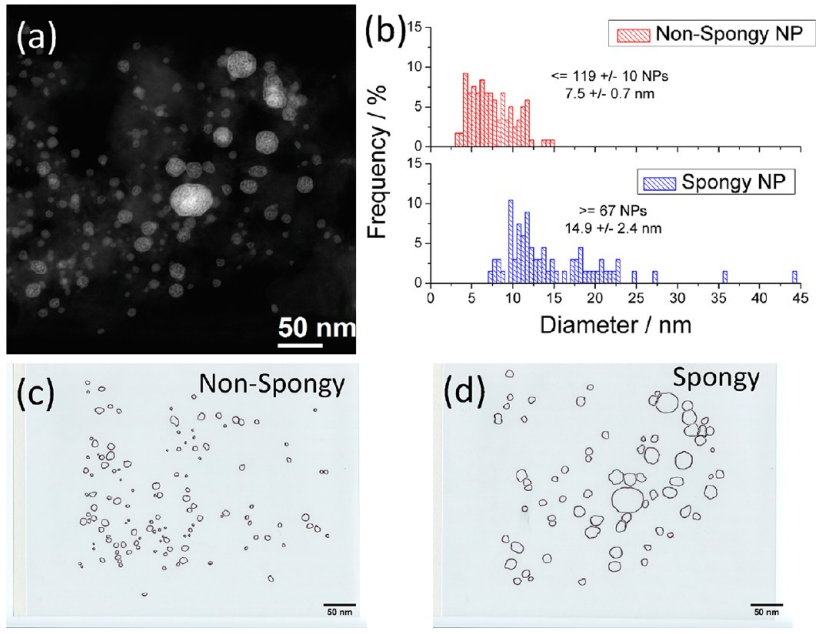

Figure 7. (a) Extend depth of field reconstruction of 34 through-focal series of the dealloyed spongy Pt−Cu nanoparticles with most nanoparticles reconstructed at the same focal plane. (b) Size distributions of nonspongy and spongy nanoparticles with error bars of mean diameter corresponding to three standard errors of the mean. (c,d) Masks for analyzing the size distribution. Each of the 34 through-focal frames is checked to categorize the spongy and nonspongy nanoparticles. However, due to the limitation of spatial resolution, we cannot eliminate errors of placing spongy ones into the nonspongy category. Therefore, we report the upper limit of nonspongy nanoparticles and the lower limit of spongy nanoparticles, assuming the confidence interval in the number of nonspongy nanoparticles is dominated by Poisson counting statistics. It is clear that larger nanoparticles are more likely to form a spongy structure.

We compared the ORR activity of spongy Pt_xCu/C nanoparticles with Pt/C. As shown in Figure 8, the as-prepared spongy particles (denoted as the "no cycling" sample) exhibited higher onset and half wave potentials than pure Pt. The half-wave potential was about 50 mV more positive than Pt. It has been reported that such hollow structures are not stable under fuel cell operating conditions.[39,44] However, after 50 cycles the ORR mass activity of the spongy nanoparticles grew by a factor of 1.6 and was even slightly higher after 5000 cycles. These data suggest that by tuning the atomic and/or electronic structures, one can achieve improved electrocatalytic activity for the ORR (Figure 8a). The CVs (Figure 8b) reveal a large hydrogen adsorption/desorption region in the first cycle but without well-resolved peaks. The hydrogen peaks decreased in amplitude

dx.doi.org/10.1021/nl302404g | *Nano Lett.* 2012, 12, 5230−5238

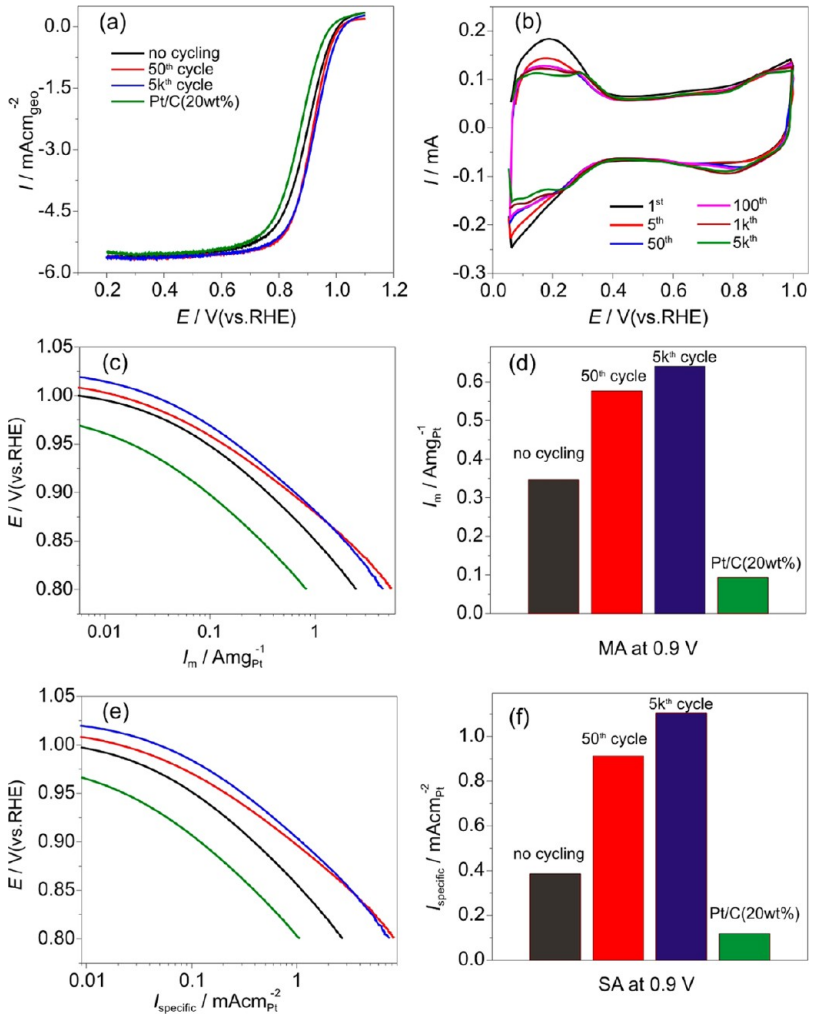

Figure 8. (a) ORR polarization curves of chemically leached nanoparticles after different potential cycles (0.05−1.0 V vs RHE) in O_2-saturated 0.1 M $HClO_4$ at a rotation rate of 1600 rpm and a scan rate of 5 mV s^{-1}. (b) Cyclic voltammograms of chemically leached nanoparticles after different potential cycles (0.05−1.0 V vs RHE) in 0.1 M $HClO_4$, at a scan rate of 5 mV s^{-1}. Color-coded legend indicates the cycle number. (c,d) Pt mass activities for the ORR at +0.9 V. (e,f) Specific activities for the ORR at +0.9 V.

with potential cycling but were almost constant after 50 cycles. In addition, two well-defined peaks appeared, indicating the presence of several Pt surface structures. This suggests that the Pt surface structure was established from the topmost layers during potential cycling. Chemical leaching gave rise to disordering of the previously ordered intermetallic nanoparticles so that the resulting surfaces would be anticipated to have more defects such as steps and kinks. With electrochemical cycling, Pt atoms associated with these defects might be able to rearrange due to electrochemical dissolution and redeposition, which may explain the appearance of the well-defined hydrogen adsorption/desorption features. This phenomenon might also lead to a change in the adsorption of oxygen-containing species and affect the ORR activity accordingly. The mass activities at +0.90 V of the spongy nanoparticles were found to be 0.35, 0.58, and 0.64 A mg^{-1}_{Pt} with no potential cycling after 50 and 5000 cycles, respectively. The corresponding specific activities were measured to be 0.38, 0.91, and 1.1 mA cm^{-2}_{Pt}. The spongy structures were stable even after 5000 potential cycles, which can be seen from the STEM images (Supporting Information Figure S6) showing that most of the spongy structures were preserved after 5000 potential cycles. The chemically leached nanoparticles exhibited better electrocatalytic activity, just after leaching, than the electrochemically treated nanoparticles after 50 cycles, as can be ascertained from Supporting Information Figure S7. The half-wave potential of the spongy product was about 20 mV more positive than the electrochemically leached product (Supporting Information Figure S7) and the mass activity at 0.9 V was about 1.5 times higher, although the specific activity is slightly less (Supporting Information Figure S7).

The higher mass activity of chemically dealloyed nanoparticles (spongy) could be attributed at least in part to the increased surface area resulting from nanovoids formed after chemical leaching. We have investigated the nature of such enhancement from two aspects. First, by comparing the CVs presented in Figures 3b and 8b, we can see that the areas corresponding to hydrogen adsorption/desorption regions are higher for chemically dealloyed nanoparticles than for electrochemically dealloyed ones, indicating that the chemically dealloyed samples present a higher electrochemical surface area (ECSA). Second, we performed high-resolution chemical mapping and 3D reconstruction of the chemically dealloyed nanoparticles (Figures 5 and 6). The results showed that the nanoparticles developed a nonporous structure after chemical dealloying. This porous structure dramatically increased the

dx.doi.org/10.1021/nl302404g | Nano Lett. 2012, 12, 5230−5238

surface-to-volume ratio which, in turn, increased the electrocatalytic activity toward the ORR.

In conclusion, ordered Cu_3Pt intermetallic electrocatalyst nanoparticles have been successfully prepared and electrochemically activated via two dealloying methods. Subangstrom resolution EELS-STEM imaging indicated that the electrochemical treatment resulted in a 3−5 monolayer Pt-rich shell, which enhanced the ORR activity. Furthermore, the chemically leached samples (spongy nanoparticles) showed both higher activity and durability for the ORR. Since most electrocatalysts yield a lower catalytic activity after extensive electrochemical aging, it is important to note that the spongy nanoparticles behaved differently with their ORR activity actually improving by electrochemical cycling, at least up to 5000 cycles. Without the aid of surfactants or capping ligands, the methods reported here offer morphology control and new opportunities for preparing durable, active and low Pt-loading electrocatalysts, which are crucial for the wide commercialization of PEMFCs.

■ ASSOCIATED CONTENT

Ⓢ Supporting Information

More experimental details, material characterizations, and additional figures (Figures S1−S6). This material is available free of charge via the Internet at http://pubs.acs.org.

■ AUTHOR INFORMATION

Corresponding Author

*E-mail: (F.J.D.) fjd3@cornell.edu; (H.D.A.) hda1@cornell.edu.

Present Address

[#]Materials Sciences Division, Lawrence Berkeley National Laboratory, Berkeley, CA 94720, United States.

Author Contributions

[▽]These authors contributed equally to this work.

Notes

The authors declare no competing financial interest.

■ ACKNOWLEDGMENTS

This work was supported by the Department of Energy though Grant DE-FG02-87ER45298 by the Energy Materials Center at Cornell, an Energy Frontier Research Center funded by the U.S. Department of Energy, Office of Science, Office of Basic Energy Sciences under Award Number DE-SC0001086. This work made use of TEM and XPS facilities of the Cornell Center for Materials Research (CCMR), under award number DMR 1120296. STEM tomography was accomplished at the National Center for Electron Microscopy, Lawrence Berkeley National Laboratory, which is supported by the U.S. Department of Energy under contract no. DE-AC02-05CH11231. Y.Y and H.L.X acknowledge the kind assistance from John Grazul and Mick Thomas from Cornell TEM facility. Y.Y also acknowledges the fellowship from American Chemical Society (ACS) Division of Analytical Chemistry (ACS) sponsored by Eastman Chemical Company. J.H.R. acknowledges the support from CCMR with funding from the Research Experience for Undergraduates program DMR-1063059.

■ REFERENCES

(1) Debe, M. K. *Nature* **2012**, *486* (7401), 43−51.
(2) Steele, B. C. H.; Heinzel, A. *Nature* **2001**, *414* (6861), 345−352.
(3) Wu, J. B.; Zhang, J. L.; Peng, Z. M.; Yang, S. C.; Wagner, F. T.; Yang, H. *J. Am. Chem. Soc.* **2010**, *132* (14), 4984−4985.
(4) Maillard, F.; Dubau, L.; Durst, J.; Chatenet, M.; Andre, J.; Rossinot, E. *Electrochem. Commun.* **2010**, *12* (9), 1161−1164.
(5) Jeon, M. K.; Zhang, Y. A.; McGinn, P. J. *Electrochim. Acta* **2010**, *55* (19), 5318−5325.
(6) Bogdanovskaya, V. A.; Tarasevich, M. R.; Kuznetsova, L. N.; Zhutaeva, G. V.; Lozovaya, O. V. *Russ. J. Electrochem.* **2010**, *46* (8), 925−933.
(7) Qian, Y. D.; Wen, W.; Adcock, P. A.; Jiang, Z.; Hakim, N.; Saha, M. S.; Mukerjee, S. *J. Phys. Chem. C* **2008**, *112* (4), 1146−1157.
(8) Yano, H.; Kataoka, M.; Yamashita, H.; Uchida, H.; Watanabe, M. *Langmuir* **2007**, *23* (11), 6438−6445.
(9) Antolini, E.; Salgado, J. R. C.; Gonzalez, E. R. *J. Power Sources* **2006**, *160* (2), 957−968.
(10) Mukerjee, S.; Srinivasan, S.; Soriaga, M. P.; McBreen, J. *J. Phys. Chem.* **1995**, *99* (13), 4577−4589.
(11) Malheiro, A. R.; Perez, J.; Villullas, H. M. *J. Electrochem. Soc.* **2009**, *156* (1), B51−B58.
(12) Wang, C.; Wang, G.; van der Vliet, D.; Chang, K.-C.; Markovic, N. M.; Stamenkovic, V. R. *Phys. Chem. Chem. Phys.* **2010**, *12* (26), 6933−6939.
(13) Wu, J.; Zhang, J.; Peng, Z.; Yang, S.; Wagner, F. T.; Yang, H. *J. Am. Chem. Soc.* **2010**, *132* (14), 4984−4985.
(14) Antolini, E.; Passos, R. R.; Ticianelli, E. A. *Electrochim. Acta* **2002**, *48* (3), 263−270.
(15) Adzic, R. R.; Zhang, J.; Sasaki, K.; Vukmirovic, M. B.; Shao, M.; Wang, J. X.; Nilekar, A. U.; Mavrikakis, M.; Valerio, J. A.; Uribe, F. *Top. Catal.* **2007**, *46* (3−4), 249−262.
(16) Sasaki, K.; Adzic, R. R. *J. Electrochem. Soc.* **2008**, *155* (2), B180−B186.
(17) Sasaki, K.; Zhang, L.; Adzic, R. R. *Phys. Chem. Chem. Phys.* **2008**, *10* (1), 159−167.
(18) Stamenkovic, V.; Markovic, N. M.; Ross, P. N. *J. Electroanal. Chem.* **2001**, *500* (1−2), 44−51.
(19) Stamenkovic, V. R.; Fowler, B.; Mun, B. S.; Wang, G.; Ross, P. N.; Lucas, C. A.; Markovic, N. M. *Science* **2007**, *315* (5811), 493−497.
(20) Mani, P.; Srivastava, R.; Strasser, P. *J. Power Sources* **2011**, *196* (2), 666−673.
(21) Oezaslan, M.; Strasser, P. *J. Power Sources* **2011**, *196* (12), 5240−5249.
(22) Strasser, P.; Koh, S.; Anniyev, T.; Greeley, J.; More, K.; Yu, C.; Liu, Z.; Kaya, S.; Nordlund, D.; Ogasawara, H.; Toney, M. F.; Nilsson, A. *Nature Chem.* **2010**, *2* (6), 454−460.
(23) Koh, S.; Strasser, P. *J. Am. Chem. Soc.* **2007**, *129* (42), 12624−12625.
(24) Srivastava, R.; Mani, P.; Hahn, N.; Strasser, P. *Angew. Chem., Int. Ed.* **2007**, *46* (47), 8988−8991.
(25) Cui, C.; Li, H.-H.; Liu, X.-J.; Gao, M.-R.; Yu, S.-H. *ACS Catal.* **2012**, *462* (6), 916−924.
(26) Liu, Z.; Xin, H. L.; Yu, Z.; Zhang, J.; Mundy, J. A.; Muller, D. A.; Wagner, F. T. *J. Electrochem. Soc.* **2012**, *159* (9), F554−F559.
(27) Casado-Rivera, E.; Volpe, D. J.; Alden, L.; Lind, C.; Downie, C.; Vázquez-Alvarez, T.; Angelo, C. D.; DiSalvo, F. J.; Abruña, H. D. *J. Am. Chem. Soc.* **2004**, *126* (12), 4043−4049.
(28) Sanabria-Chinchilla, J.; Abe, H.; DiSalvo, F. J.; Abruña, H. D. *Surf. Sci.* **2008**, *602* (10), 1830−1836.
(29) Xin, H. L.; Mundy, J. A.; Liu, Z.; Cabezas, R.; Hovden, R.; Kourkoutis, L. F.; Zhang, J.; Subramanian, N. P.; Makharia, R.; Wagner, F. T.; Muller, D. A. *Nano Lett.* **2011**, *12* (1), 490−497.
(30) Wang, D.; Xin, H. L.; Yu, Y.; Wang, H.; Rus, E.; Muller, D. A.; Abruna, H. D. *J. Am. Chem. Soc.* **2010**, *132* (50), 17664−17666.
(31) Yu, Y. X.; H., L.; Hovden, R.; Wang, D.; Rus, E.; Mundy, J. A.; Muller, D. A.; Abruna, H. D. *Nano Lett.* **2011**, DOI: DOI: 10.1021/nl203920s.
(32) Carlton, C. E.; Chen, S.; Ferreira, P. J.; Allard, L. F.; Shao-Horn, Y. *J. Phys. Chem. Lett.* **2012**, *3* (2), 161−166.
(33) Crewe, A. V.; Wall, J.; Langmore, J. *Science* **1970**, *168* (3937), 1338−1340.
(34) Markovic, N. M.; Ross, P. N. *Surf. Sci. Rep.* **2002**, *45* (4−6), 121−229.

(35) Mukerjee, S.; Srinivasan, S.; Soriaga, M. P.; McBreen, J. *J. Phys. Chem.* **1995**, *99* (13), 4577−4589.
(36) Vidal-Iglesias, F. J.; Aran-Ais, R. M.; Solla-Gullon, J.; Herrero, E.; Feliu, J. M. *ACS Catal.* **2011**, *2* (5), 901−910.
(37) Chen, Q.-S.; Solla-Gullon, J.; Sun, S.-G.; Feliu, J. M. *Electrochim. Acta* **2010**, *55* (27), 7982−7994.
(38) Cueva, P.; Hovden, R.; Mundy, J. A.; Xin, H. L.; Muller, D. A. *Microsc. Microanal.* **2012**, DOI: DOI: 10.1017/S1431927612000244.
(39) Chen, H. M.; Liu, R.-S.; Lo, M.-Y.; Chang, S.-C.; Tsai, L.-D.; Peng, Y.-M.; Lee, J.-F. *J. Phys. Chem. C* **2008**, *112* (20), 7522−7526.
(40) Oezaslan, M.; Heggen, M.; Strasser, P. *J. Am. Chem. Soc.* **2012**, *134* (1), 514−524.
(41) Hovden, R.; Xin, H. L.; Muller, D. A. *Microsc. Microanal.* **2011**, *17* (01), 75−80.
(42) Forster, B.; Van de Ville, D.; Berent, J.; Sage, D.; Unser, M. *Microsc. Res. Tech.* **2004**, *65* (1−2), 33−42.
(43) Erlebacher, J.; Aziz, M. J.; Karma, A.; Dimitrov, N.; Sieradzki, K. *Nature* **2001**, *410* (6827), 450−453.
(44) Peng, Z.; Wu, J.; Yang, H. *Chem. Mater.* **2010**, *22* (3), 1098−1106.

■ NOTE ADDED AFTER ASAP PUBLICATION

This paper was published ASAP on September 10, 2012. The symbol for Author Contributions has been corrected. References 1 and 40 have been updated. The revised version was posted on September 17, 2012.